Stability of colloidal gas aphrons based on polymer-surfactant formulations and molecular dynamics insights

Ayaulym Amankeldiyeva, Samal Kaumbekova, Aigerim Khalidulliyeva, Zhanat Salimova, Aizhan Ibrayeva, Maxime Cochennec, Stéfan Colombano, Yerlan Amanbek, Yanwei Wang, Sagyn Omirbekov

To cite this version:

Ayaulym Amankeldiyeva, Samal Kaumbekova, Aigerim Khalidulliyeva, Zhanat Salimova, Aizhan Ibrayeva, et al.. Stability of colloidal gas aphrons based on polymer-surfactant formulations and molecular dynamics insights. Scientific Reports, 2025, 15 (1), pp.23480. ⟨10.1038/s41598-025-08100-4⟩. ⟨hal-05173810⟩

HAL Id: hal-05173810

https://brgm.hal.science/hal-05173810v1

Submitted on 21 Jul 2025

scientific reports

Check for updates

Stability of colloidal gas aphrons based on polymer-surfactant formulations and molecular dynamics insights

Ayaulym Amankeldiyeva[1,2], **Samal Kaumbekova**[1], **Aigerim Khalidulliyeva**[1,2], **Zhanat Salimova**[1,2], **Aizhan Ibrayeva**[1], **Maxime Cochennec**[4], **Stéfan Colombano**[4], **Yerlan Amanbek**[3], **Yanwei Wang**[1,2] & **Sagyn Omirbekov**[1]✉

Colloidal gas aphrons (CGAs) are promising fluids for environmental remediation due to their stability, high viscosity, and effective gas transport. However, previous studies have been limited by narrow concentration ranges, leaving key mechanisms behind bubble stability insufficiently understood. This study systematically explores bubble stability across a wide range of xanthan gum (XG) and sodium dodecyl sulfate (SDS) concentrations (1–10× CMC and 1000–10,000 ppm) using advanced AI-assisted image analysis and molecular dynamics (MD) simulations. AI-enhanced microscopy enabled precise quantification of bubble size and morphology, while MD provided molecular-level insights into surfactant-polymer interactions at bubble interfaces. Results showed optimal CGA stability at specific surfactant-polymer ratios, significantly reducing gas diffusion and bubble coalescence. These integrated experimental and computational methods offer valuable guidelines for designing robust CGA-based remediation fluids.

Keywords Colloidal gas aphrons, Surfactant, Polymer, Stability, Image analysis, Molecular dynamics simulation

Complex aqueous fluids like foams and polymers have shown the potential to improve sweeping efficiency in heterogeneous porous media commonly used in enhanced oil recovery (EOR)[1] and, more recently, in soil remediation applications[2,3]. Due to their non-Newtonian behavior, these fluids can lead to a more uniform displacement of injected fluid, reducing the effect of variations in the permeability of porous media[4–6]. Specifically, foam applications have attracted great attention due to their large gas fraction, extensive surface area, and advantages as a gas carrier. However, foam stability, especially when displacing oil or contaminants, is a weak point that depends on factors such as the type of surfactant, gas, and bubble size[7,8]. Additionally, foam injection in porous media is hindered in soil remediation applications due to its compressibility effect, which can lead to soil lifting under certain pressure. Polymers, on the other hand, behave more predictably and are frequently the recommended choice for in-situ soil remediation[9]. Nevertheless, foams have the unique advantage of transporting gases, which can enhance biodegradation by aerobic bacteria. Hence, a fluid alternative to foam can be considered colloidal gas aphrons (CGAs), which have a lower gas fraction compared to foam, thus exhibiting lower compressibility. Despite these advantages, the precise relationship between CGA formulation, bubble stability, and performance in environmental remediation remains poorly understood, especially at concentrations beyond traditionally studied ranges.

CGAs are also known as microfoams that can be an alternative to conventional foams. CGAs were first introduced by Sebba in 1971, and they consist of microbubbles (10–100 µm in diameter) with a gaseous core encapsulated by surfactant multilayers[10]. They have large surface areas and water-like flow characteristics, which make them unique and suitable for soil remediation applications[11]. CGAs are widely used as transport fluids to deliver oxygen, bacteria, and dissolved minerals for environmental applications[12]. The primary effectiveness of CGAs is based on their stability. This stability is affected by numerous factors, including the properties of the

[1]Center for Energy and Advanced Materials Science, National Laboratory Astana, Nazarbayev University, Astana, Kazakhstan. [2]Department of Chemical and Materials Engineering, School of Engineering and Digital Sciences, Nazarbayev University, Astana, Kazakhstan. [3]Department of Mathematics, School of Sciences and Humanities, Nazarbayev University, Astana, Kazakhstan. [4]BRGM, F-45060 Orléans, France. ✉email: sagyn.omirbekov@nu.edu.kz

encapsulating shell, gas hold-ups, surface tension, pH, preparation conditions, and the types and concentrations of polymers and surfactants[13].

Experimental studies have shown the effects of polymer and surfactant concentrations on CGA stability. For instance, Pasdar et al.[14] compared the performance of CGAs made with two anionic surfactants (SDBS, sodium dodecylbenzene sulfonate, and SDS, sodium dodecyl sulfonate) and noted the effect of increasing the concentrations of the polymer and surfactant on the stability. Le et al.[15] studied CGAs generated with 1000, 2500, and 4000 ppm Xantham Gum (XG) concentrations. They found that XG concentrations significantly impacted CGA stability, and the highest stability was obtained at 4000 ppm. Shi et al.[16] described the effect of XG polymer concentration at a wider range (1000–7000 mg/L) in combination with a hydroxyl sulfobetaine surfactant. They observed that CGA stability was not significantly affected by XG concentrations above 6000 mg/L, although a concentration above 7000 mg/L was not examined in the study. They also found that the stability of microbubbles increased with surfactant concentration and stirring range but decreased with rising salinity. Similarly, according to the study by Keshavarzi et al.[17–19]increasing polymer concentration positively affected CGA's stability. When XG concentration increased from 0.1 to 0.3 wt%, the half-life increased 5 times. However, they noted that the upper limit of polymer concentration and viscosity should be determined by the pumping ability of the fluid as well as its removal ability. To evaluate the surfactant effect, they measured the dynamic changes in surface tension for aqueous solutions of SDS, CAPB, and Triton X-100 in the presence of 0.1 wt% XG, where both CAPB and Triton X-100 showed lower equilibrium surface tension values compared to SDS. Furthermore, large volumes of CGA were obtained for SDS solutions, whereas only small amounts were obtained for CAPB and Triton X-100. Other research highlights the importance of surfactant type and polymer concentration, indicating that the interplay between these components is crucial[17–19].

Nevertheless, bubble size analysis remains a key parameter for assessing CGA stability. Many techniques were employed to investigate bubble size distribution and other stability parameters, such as image analysis[20]CCD camera imaging[21]and advanced image processing[22,23]. Traditional bubble characterization methods rely on subjective manual measurements, limiting accuracy and reproducibility. Recent advancements in AI-assisted image analysis promise higher precision and consistent quantification of bubble populations[24]. Moreover, understanding the interactions among bubbles is critical for analyzing CGA stability. To optimize the application of CGAs, it is crucial to understand the interactions between microfoam bubbles and bulk medium. Hence, Molecular Dynamics (MD) simulations recently started to be a valuable tool for studying the interfacial properties of microfoams and their molecular-level interactions. For instance, the effect of water-soluble environmentally friendly polyvinyl alcohol (PVA) polymer on the foaming ability of anionic surfactants was studied via MD simulations[25]. According to the results of this study, PVA with a hydrophobic tail improved the foaming ability of sodium decyl sulfate (SDeS) surfactant by enhancing the hydration of hydrophilic head groups of the surfactants and producing an H-bond network. Similarly, recent MD studies in the literature investigated the individual and synergistic effects of surfactants, polymers, solvents, ions, pH, and salinity on the foaming abilities and foam stability. For example, the MD study[26] examined the properties of ultra-stable aqueous foams with multilayer films stabilized by solvents, such as 1-dodecanol (DDA), SDS, and PVA. Notably, the results of the MD study showed the combined effect of SDS, DDA, and PVA, which could increase the distribution intensity of bound water molecules in foam film layers associated with the formation of ultra-stable aqueous foams. Furthermore, the synergistic effect of alkali, surfactant, and environmentally friendly polymer on the formation and stabilization of water-based foam was studied by MD simulation performed[27]. Based on the results of this study, an increase in the pH, SDBS surfactant concentration, and HPAM (Hydrolyzed Polyacrylamide, environmentally friendly polymer) concentration resulted in an improved stability of the foam liquid film.

To our knowledge, no previous studies have combined AI-assisted quantitative image analysis with molecular dynamics simulations to systematically investigate CGA stability across broad surfactant-polymer concentration ranges. This approach provides comprehensive insights into bubble size, morphology, and molecular interactions, significantly advancing the understanding and optimization of CGA formulations for practical environmental remediation applications.

Therefore, our objective is to enhance understanding of the synergistic effects between XG and SDS on bubble stability and to examine a broader range of XG and SDS concentrations. By utilizing advanced AI tools for image analysis, we aim to detect and quantify more bubbles with greater precision, significantly reducing the time required for analysis compared to traditional methods. Additionally, MD simulations will reveal the molecular mechanisms behind the enhanced viscosity provided by XG, demonstrating how its dense molecular network effectively inhibits gas movement.

This integrated approach, combining experimental data, AI-based image analysis, and computational MD modeling, introduces a new paradigm for studying complex systems like CGAs. By revealing the synergistic interactions between XG and SDS, this study advances our understanding of CGA stability. It establishes the foundation for their optimal use in soil remediation and other environmental fields.

Materials and methods

Fluid preparation

Materials

In this study, we used Xanthan Gum (XG) polymer and Sodium Dodecyl Sulfate (SDS) surfactant as the two main components for CGA generation. The XG polymer powder (Sigma-Aldrich, molecular weight > 1,000,000 g/mol) was selected due to its high viscosifying capacity, biocompatibility[28], and proven effectiveness in environmental remediation studies[29].

SDS powder (Sigma-Aldrich, 98.5% purity) was utilized, with a critical micelle concentration (CMC) experimentally determined in our laboratory as 0.23 ± 0.01% (w/w).

Preparation of the base solution

The XG polymer powder was fully dissolved by hydration in distilled water to prepare the base solution. First, we measured the required amount of XG powder for different concentration values: 1000, 2000, 4000, 6000, 8000, and 10,000 ppm. Then, this particular amount of XG was added to 100 mL of distilled water. Due to the high viscosity of XG solutions, complete polymer dissolution was achieved by vigorous stirring at 8000 rpm for 20 min using a Silverson L5M-A overhead stirrer[20,30,31].

CGA generation

In order to generate CGA, the base solution was mixed with an aphron stabilizer, an anionic surfactant SDS. The SDS powder was promptly added to the well-homogenized base fluid and stirred for two minutes at the same rotation speed of 8000 rpm[32]. Surfactant concentrations of 1, 2, 4, 6, 8, and 10 CMC were systematically selected to span a broad range, enabling comprehensive assessment of their effect on CGA dispersion quality and stability. In total, we prepared six concentrations of XG as base solutions, and each experimental condition was replicated three times to ensure reproducibility. Six concentrations of SDS surfactants were added to each base solution, resulting in a total of 36 CGA samples. Due to frictional heating during high-speed mixing, CGA sample temperatures rose, ranging between 313.15 K and 328.15 K, and were monitored consistently using a calibrated digital thermometer (± 0.5 K accuracy). All mixing was performed at ambient atmospheric pressure. Then, the generated CGAs were examined using microscopy.

Microscopic examination

The generated CGAs were examined using a Zeiss digital microscope (Axio Zoom V16, Carl Zeiss Microscopy GmbH) equipped with a charge-coupled device (CCD) camera (Axiocam 506 mono). Bubble size analysis was performed to assess the stability of the CGAs by observing the distribution of bubble sizes over time. Sample images were captured using a CCD camera, following procedures adapted from Pasdar et al.[21]. All samples were imaged at 40× magnification. Images were acquired as Z-stacks comprising 21 optical slices per sample to capture the bubble structure in three dimensions, as shown in Fig. 1a. Each image had a resolution of 2752 × 2208 pixels and was recorded at a 14-bit depth (uint16). Display intensity was adjusted linearly between pixel values of approximately 0.07 and 0.19 to enhance visual contrast before image processing. Each sample, containing approximately 800 to 2500 bubbles at the surface of all layers (Fig. 1b), was recorded every ten minutes for one hour. These images were subsequently analyzed using AI-based segmentation tools as detailed in "Image analysis" section.

Image analysis

Software and equipment.

Deep learning AI was used via Biodock software to selectively segment bubbles and analyze the bubble size distribution over time under different CMC and CGA conditions in a subset of microscopy images[33]. Approximately 200 microscopy images (each covering an area of 3132.52 × 2506.08 μm[5]) were systematically analyzed using the Biodock AI platform over a five-day processing period. Examples of segmented pictures taken at the initial time and after 60 min are presented in Fig. 2.

Analysis of microscopy images with Biodock

Image clustering approach

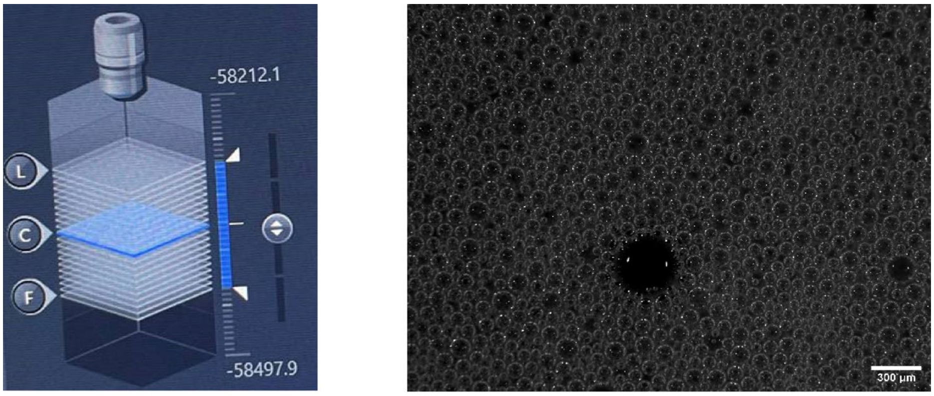

a) b)

Fig. 1. CGA sample with XG polymer at1000 ppm and SDS surfactant at 8 CMC: (**a**) Z-axis measurement tool for all 21 layers; (**b**) 40× zoom of bubbles in the central layer.

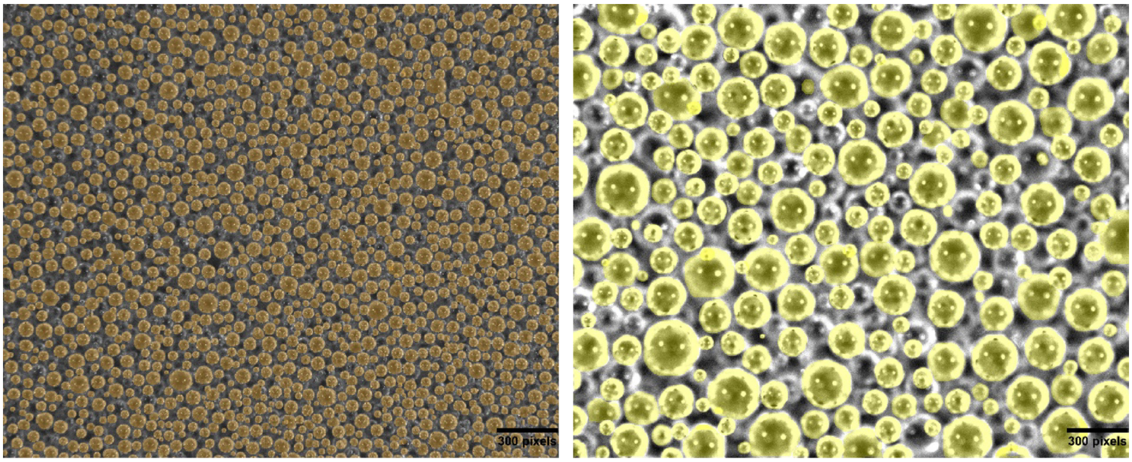

a) b)

Fig. 2. Example of segmented CGA image at 4 CMC 6000 ppm using Biodock Software Platform 2024[33]: (**a**) CGA bubbles (t = 0 min); (**b**) CGA bubbles (t = 60 min).

Microscopic images of bubbles were clustered into three categories based on the following criteria:

- Bubble size: approximate size of individual bubbles.
- Bubble count: number of bubbles within the region of interest (ROI).
- Image quality: degree of clarity, including sharp or blurred regions.

This classification enabled the development of three specialized AI models tailored to different experimental conditions, enhancing the precision of bubble detection across varied scenarios. The subset of data (~ 7% of the total dataset) was separated for training all three models, and 7% of the data was used for testing the models' performance. To improve model generalization and robustness, data augmentation techniques were applied during training, including random horizontal and vertical flips, brightness and contrast adjustments, random rotations, and random rescaling.

All three models were implemented using the Multi-Path Vision Transformer (MPViT) architecture, a state-of-the-art backbone for dense prediction tasks such as object detection and segmentation[34] Mpvit: Multi-path vision transformer for dense prediction. In Proceedings of the IEEE/CVF conference on computer vision and pattern recognition (pp. 7287–7296).). MPViT is designed to capture fine and coarse features at the same resolution by using multi-scale patch embedding and a multi-path Transformer structure. Each path processes patches of different scales independently and then aggregates the resulting features, enabling robust multi-scale feature representation[47]. For data labeling, Biodock's "AI Select" and "AI Detect" tools were employed, which are built upon Meta's Segment Anything Model.

AI models for bubble detection

Model 1: detection of crowded and tiny bubbles

Model 1 was designed to identify more diminutive and more densely packed bubbles, typically found in the early stages of the experiment. Occasionally, large bubbles were observed, often surrounded by tiny bubbles. The tile size for this model was chosen as $1135 \times 1135\ \mu m^2$. Six representative images were selected based on the complexity of bubble distribution (varying sizes and densities), ensuring the AI models were effectively trained for diverse bubble populations. The photos contained mostly crowded and comparatively small bubbles (mean area of approximately $5000\ \mu m^2$). However, some images featured huge bubbles (area > $50000\ \mu m^2$) surrounded by significantly smaller ones (area < $500\ \mu m^2$), which posed challenges for the AI model to segment all bubbles accurately. In addition to AI-based selection, manual pen correction was occasionally necessary in these complex regions to ensure precise delineation of the bubble boundaries.

Model 2: detection of larger bubbles

Model 2 was trained to detect larger bubbles. Occasional tiny bubbles appearing inside larger ones were disregarded, as only the uppermost layer of bubbles was analyzed. Second-layer bubbles were excluded from consideration. The tile size was chosen as $2270 \times 2270\ \mu m^2$ to minimize the fragmented bubbles. Three different images belonging to three different conditions were chosen, and one tile was labeled for each image. AI select, and AI detects methods were used for labeling.

Model 3: mixed conditions, lower quality image

Model 3 was trained to handle images exhibiting mixed conditions, where bubble size and image quality varied significantly. These images, often containing blurred regions in the ROI, were manually pre-processed by adjusting the channel settings. Some images were discarded from the analysis due to their low quality. 1135 × 1135 μm^2 tiles were chosen for this model. The training was performed on five labeled regions across five images, with two labeled tiles per image.

All bubbles in the training images were labeled as an object-type class for all models. The proportion of the predicted objects that match the labels put in manually or by bounding box at different thresholds averaged over all the objects in that group, identifies the model's accuracy and is called average precision (AP). The mean AP for all bubble sizes was 95.4, 91.7, and 90.3 for model 1, model 2, and model 3, respectively. While MPViT-based models provided high segmentation accuracy across varied experimental conditions, a key limitation is their inference latency. Due to the multi-path structure, MPViT experiences slower runtime compared to some single-path models (e.g., Swin-T or XCiT-S12/16). This is attributed to suboptimal GPU utilization, including context switching and kernel synchronization, similar to the challenges observed in grouped convolutions. Efforts are ongoing to address this limitation through more efficient implementation strategies[21].

Parameters for stability analysis at micro-scale

Stability analysis requires fundamental parameters to enable comparison. For this, the resulting segmented microscopic images from the AI tools provided values for bubble size and bubble count: Mean Bubble Area (MBA) and Number of bubbles (Nb). MBA accounts for the average size of the bubbles within the image of the CGA solution, which serves as an indicator of uniformity and stability. Nb quantifies the total count of bubbles in an image, advocating for the persistence and coalescence of the gas phase over time. MBA and Nb were computed using standard image processing protocols, applying edge-correction algorithms and size filtering (removing objects smaller than a minimum detectable size) to ensure accuracy and consistency. These parameters assist in describing the main tendencies of each concentration of XG and SDS: MBA reveals bubble growth over time, and Nb reflects bubble breakdown or aggregation. After extracting the data using AI machine learning, the K-means clustering became crucial in categorizing the data. K-means clustering allowed the grouping of concentrations with common tendencies and revealed trends in CGA stability across time.

MD simulations

Intermolecular interactions and movement of gas molecules in CGA models

Atomistic MD simulations were conducted using the Gromacs 2022 software[35] with the gromos54a7 forcefield, selected for its reliable representation of surfactant-polymer interactions, including SDS and carbohydrate-based molecules[36,37]. This force field has been widely used in similar systems and provides a good balance between computational efficiency and accuracy. Two SDS monolayers were used to mimic the CGA interface positioned on the surface of the water slab (Fig. 3).

The SPC water model was used in the water slab, selected due to its computational efficiency and widespread use in studies involving surfactants and polymer systems, including SDS-containing systems[38]. A simulation box with dimensions of 6*6*30 nm^3 was used to model the lamella in which the water slab and SDS monolayers were positioned in the center. The negatively charged SDS was neutralized by Na^+ ions, inserted in the water slab. The required number of ions and molecules was inserted into the simulation box, according to Table 1, keeping the

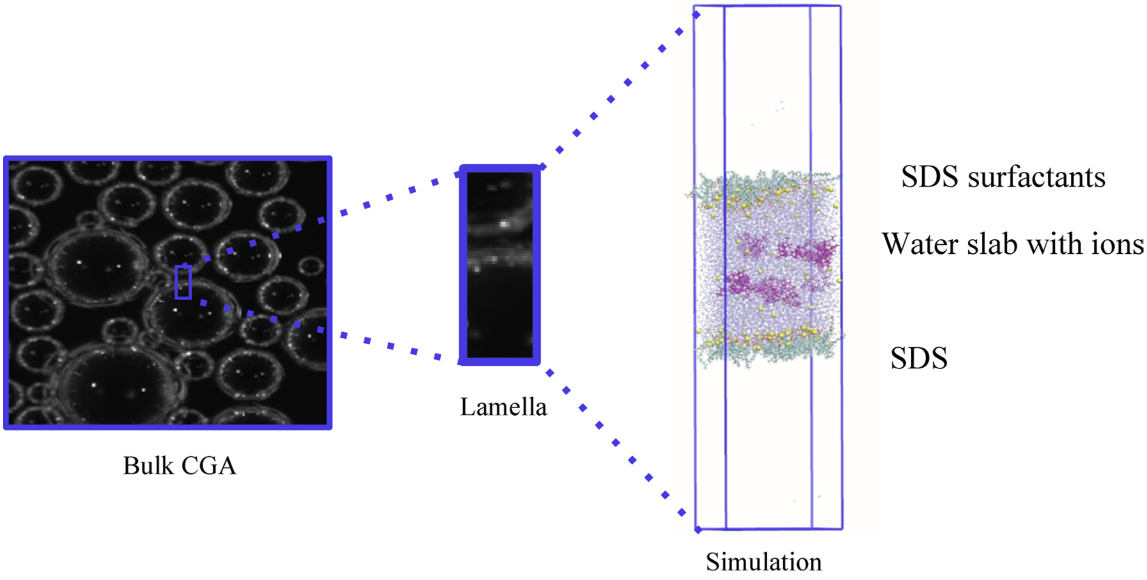

Fig. 3. A representative snapshot of the simulation box with the dimensions of 6*6*30 nm^3.

Simulated system	N_2	SDS	Na^+	H_2O	XG	XG concentration
1	0	128	128	10,263	0	0
2	0	128	128	9919	8	12 g/L (0.012 M)
3	0	128	128	9429	16	24 g/L (0.024 M)
4	0	128	128	7946	24	36 g/L (0.036 M)
5	30	128	128	10,211	0	0
6	30	128	128	9873	8	12 g/L (0.012 M)
7	30	128	128	9380	16	24 g/L (0.024 M)
8	30	128	128	7905	24	36 g/L (0.036 M)
9	30	0	0	9491	16	24 g/L (0.024 M)
10	30	64	64	9191	16	24 g/L (0.024 M)

Table 1. Molecular composition of MD simulation systems, detailing molecule counts alongside their mass (g/mol) and molar concentrations (M), ensuring clarity and reproducibility.

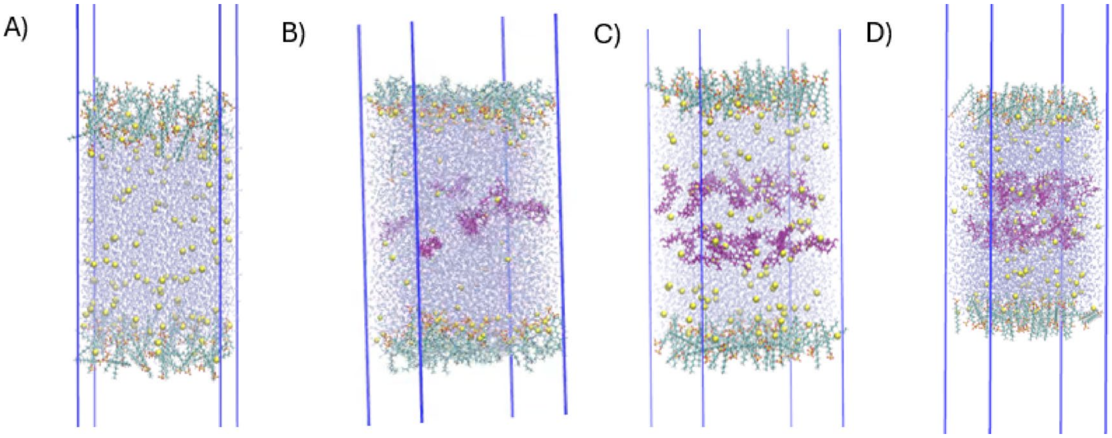

Fig. 4. Representative snapshots of the simulated systems at the beginning of the simulations with constant SDS concentration and varied XG concentrations: (**A**) 128 SDS : 0 XG, (**B**) 128 SDS : 8 XG, (**C**) 128 SDS : 16 XG, (**D**) 128 SDS : 24 XG. Representation style and methods of coloring: XG: purple (licorice), Na^+: yellow (VDW), H_2O: transparent blue (CPK), SDS atoms (licorice): C: cyano, H: white, O: red.

SDS and Na + ions concentration at 0.20 M in all simulated systems at various XG concentrations. XG monomers (C36H58O29P2) were inserted in the center of the water slab to mimic the presence of polymer segments. Due to the simulation box size limitations, up to 24 XG monomers were used for the MD simulations, mimicking the presence of XG polymer segments at different concentrations. The forcefield parameters and structures of the molecules and ions were taken from Automated Topology Builder databases[39].

After filling the box with a required number of molecules, energy minimization was performed, with a constraint of maximum force to be less than 100 kJ/mol/nm on any atom, to optimize the starting configuration of the simulation box. Following energy minimization, the canonical ensemble at constant temperature and volume (NVT) was conducted with a V-rescale thermostat for 0.25 ns at 323 K. The simulation temperature (323 K) aligns with typical conditions from our laboratory experiments, providing direct comparability between simulation and experimental results. Finally, the production runs for each system was performed for 50 ns at NVT conditions at 323 K with the time step of 1 fs. During the simulations, all bonds were constrained with the LINCS algorithm. Furthermore, periodic boundary conditions (PBC) in all directions were applied for all simulations. All systems were simulated three times. The output parameters were saved each one ps. To visualize and study the simulation results Visual Molecular Dynamics (VMD) tool was used[40]. The results of the simulations were analyzed via the Gromacs package using density, mean-square displacement (MSD), and radial distribution function (RDF) analyses.

Two simulation conditions were examined based on the presence of N_2: (1) systems without N_2, where the concentration of SDS was fixed while varying the concentration of XG, and (2) systems with varying concentrations of both SDS and XG in the presence of N_2. Representative snapshots of the visualized systems at the beginning of the simulations are displayed in Figs. 4 and 5, illustrating the systems without N_2 and with N_2, respectively.

The vacuum layers of the simulation boxes are shortened, and the simulation box borders are not shown for better clarity. Figure 3 shows a representative snapshot of the simulation box with borders and the full-size vacuum layers.

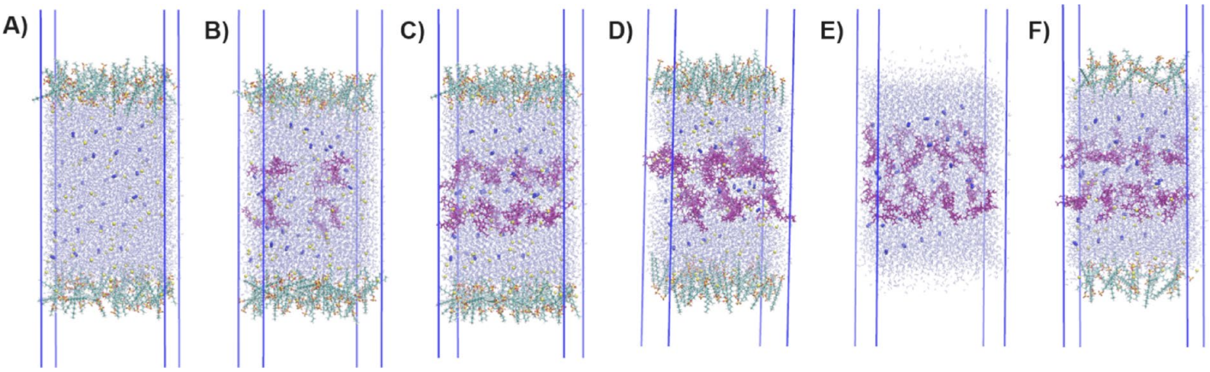

Fig. 5. Representative snapshots of the simulated systems at the beginning of the simulations with N_2 gas movement from the water slab to vacuum layers at various concentrations of SDS and XG: (**A**) 30 N_2 in 128 SDS : 0 XG, (**B**) 30 N_2 in 128 SDS : 8 XG, (**C**) 30 N_2 in 128 SDS : 16 XG, (**D**) 30 N_2 in 128 SDS : 24 XG, (**E**) 30 N_2 in 0 SDS : 16 XG, and (**F**) 30 N_2 in 64 SDS : 16 XG. Representation style and methods of coloring: XG: purple (licorice), Na^+: yellow (VDW), N_2 : dark blue (VDW), H_2O: transparent blue (CPK), SDS atoms (licorice): C: cyano, H: white, O: red.

In the conditions with N_2, 30 Nitrogen molecules were added to the water slab to monitor the kinetics of the diffusion of gas molecules from the aqueous phase to the vacuum phase. To investigate the effect of XG concentration on the gas movement, XG monomers were inserted in the center of the water slab, varying the number of XG monomers from 0 to 8, 16, and 24 molecules in the presence of 128 SDS molecules, as shown in Fig. 5A–D, respectively. In addition, the effect of SDS concentration on the gas movement was studied by varying the total number of the SDS molecules in the surfactant monolayers from 0 to 64 and 128 in the presence of 16 XG monomers, as shown in Fig. 5E–F, respectively. The required number of ions and molecules was inserted into the simulation box, according to Table 1. The percentage distribution of N_2 molecules in the vacuum layer was reported within 25 ns of the simulation. The results were averaged among three runs for each system under the study.

Movement of gas molecules in bulk phase

Furthermore, the movement of N_2 molecules was studied in the aqueous bulk phase, in the absence of the vacuum phase. SDS and XG monomer molecules were randomly inserted into the simulation boxes with the size of 10*10*10 nm[6]. SPC water model was used for the solvation of the simulation box. To investigate the effect of XG concentration on the movement of gas molecules, the number of the XG monomers was varied from 0 to 8, 16, and 24 molecules, in the presence of 128 SDS molecules. The representative snapshots of the simulation boxes at the beginning of the simulations are shown in Figure S4A-D, respectively. The required number of ions and molecules was inserted into the simulation box, according to Table S1. After filling the box with a required number of molecules, energy minimization was performed, with a constraint of maximum force to be less than 100 kJ/mol/nm on any atom, to optimize the starting configuration of the simulation box. Following energy minimization, the NVT step was conducted with a V-rescale thermostat for 0.25 ns at 323 K. Next, the NPT equilibration was performed at constant pressure of 1 bar with a V-rescale thermostat and a C-rescale barostat for 0.25 ns at 323 K. Finally, the production runs for each of the systems were performed for 25 ns at 323 K with the time step of 1 fs. During the simulations, all bonds were constrained with the LINCS algorithm. MD simulations were carried out for 25 ns at 323 K and 1 bar, using V-rescale thermostat and C-rescale barostat for temperature and pressure control, respectively. PBC were applied in XYZ-directions for all simulations. The output parameters were saved each 1 ps. The movement of gas molecules was characterized by MSD of N_2 molecules within the first 10 ns of the MD simulation runs. The results were averaged among three runs for each system under the study.

Results and discussion

This section presents the key experimental results and discusses the mechanisms influencing the stability of CGAs. Firstly, we examine how different concentrations of XG and SDS impact the initial formation and properties of CGAs. Subsequently, we analyze the temporal evolution of CGA stability by assessing bubble growth, size distributions, and their relationship to polymer-surfactant interactions. Finally, insights gained from molecular dynamics simulations shows the molecular-level interactions that support observed macroscopic stability behaviors.

Effect of SDS and XG on CGA generation

Figure 6 shows the initial bubble characteristics, specifically mean bubble area (MBA, in μm^2) and bubble count (Nb), across various CGA formulations at the time of generation (t = 0), highlighting the influence of XG and SDS concentrations.

Figure 6a illustrates the initial values of the MBA (MBA_0) and Nb (Nb_0) for 30 CGA samples with different concentrations of XG and SDS (with CMC values indicated by numbers) based on the K-means

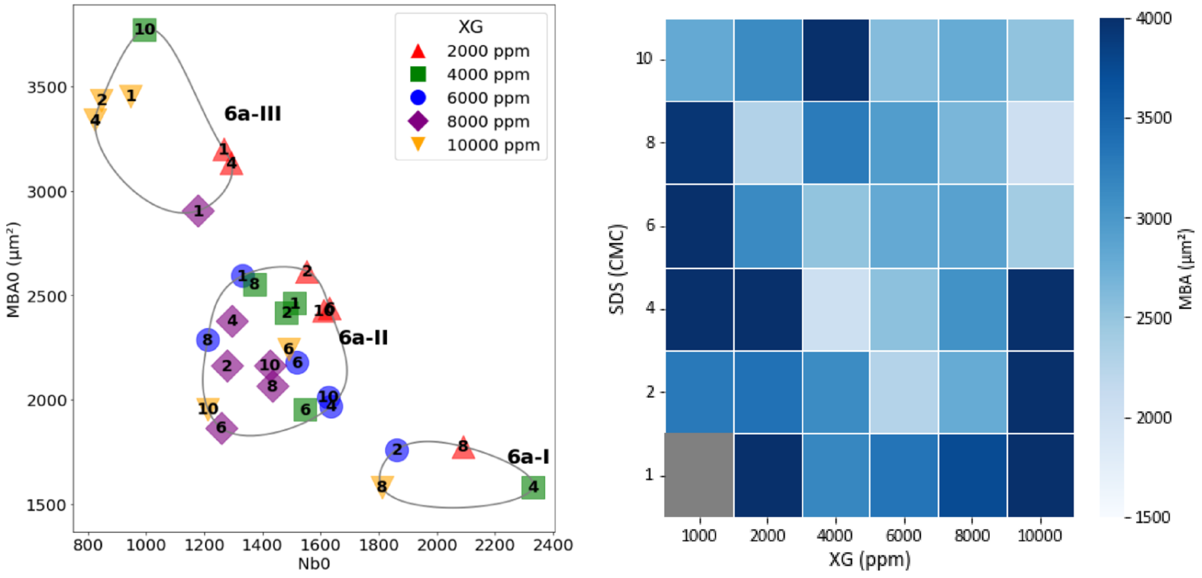

a)

b)

Fig. 6. Initial MBA and Nb values: (**a**) MBA$_0$ vs. Nb$_0$ for various concentrations of CGA, (**b**) Color map on MBA for 36 concentrations.

clustering approach. The plot features 30 CGA samples, excluding the 1000 ppm XG concentration for all CGAs due to its unstable behavior. This graphical representation is essential for demonstrating CGA generation. A clear relationship emerged between initial bubble size, number of bubbles, and the formed clusters, indicating that polymer-surfactant concentrations significantly influence initial CGA characteristics.

The analysis reveals three distinct clusters:

- *Cluster 6a-I* shows concentrations of XG and SDS with the highest Nb_0 values, but the lowest MBA_0 values within the specified range.
- *Cluster 6a-II* highlights concentrations where both Nb_0 and MBA_0 values fall in the middle of their respective ranges (mid-MBA$_0$ and mid-Nb$_0$). It also features the widest variety of combinations of polymer and surfactant concentrations.
- *Cluster 6a-III* represents concentrations with the lowest Nb_0 values but with the largest MBA_0.

For further analysis, cluster 6a-II, positioned at mid-MBA$_0$ and mid-Nb$_0$ data points, was selected for stability analysis. This choice ensured excellent stability, as it facilitates uniform bubble formation by bubble sizes.

Figure 6b presents a color map of the MBA for all 36 concentrations of CGA, illustrating the MBA range with a color bar at 0 min. The range of MBA can be seen through color bars starting from 1500 to 4000 µm^2. The gray area in 1 CMC, corresponding to the 1000 ppm concentration, indicates instability in the system at the initial stage. Several darker areas show concentrations whose bubbles were generated at a larger size immediately at the generation stage than the others. Specifically, the CGA generated at lower XG concentrations, such as 1000 ppm and 2000 ppm, exhibited a larger MBA. The largest MBA was obtained by 4 CMC 1000 ppm, accounting for 5065 µm^2. This behavior aligns with previous findings on the influence of salts and temperature on XG solution viscosity, which increases significantly with higher XG concentrations[41]. Their study measured the zero-shear viscosity of XG aqueous solutions at fixed ionic concentrations. Furthermore, various viscosity parameters (relative viscosity, reduced viscosity, inherent viscosity, and specific viscosity) were calculated. It was found that relative viscosity increased with higher XG concentrations due to the repulsive Coulombic interactions between charged groups on the side chains. In our study, lower XG concentrations (1000–2000 ppm) resulted in lower solution viscosity, reducing resistance to bubble growth, thus producing larger initial bubble areas compared to higher viscosity formulations. Additionally, concentrations of 1, 2, and 4 CMC at 10,000 ppm also demonstrated high MBA at the generation stage, with values of 3453 µm^2, 3433 µm^2, and 3338 µm^2, respectively.

Figure 7 illustrates the gas fraction in the CGA system at 0 min for all 36 concentrations. The gas fraction values represent the ratio of gas volume in the solution to the total volume of liquid and gas in the system. Based on the gas fraction, the solutions can be classified as follows: dry (gas fraction > 0.99), wet (0.64 < gas fraction < 0.99), and bubbly fluid (gas fraction < 0.64)[4]. The gas fraction was determined by dividing the total area of the bubbles by the area of the image for the given system of CGA bubbles. The area of the image was taken as 3132.52 × 2506.08 µm. According to the results, solutions with XG concentrations of 2000 ppm and 4000 ppm can be classified as wet, while higher XG concentrations present bubbly fluid solutions.

The analysis shows a decreasing trend in this value as the concentration of XG increases. As the viscosity of the solution increases with rising XG concentration[41]the processes of bubble formation and motion are resisted. Bubbles appear smaller at high XG concentrations such as 6000, 8000, and 10,000 ppm, as shown in Figure S1

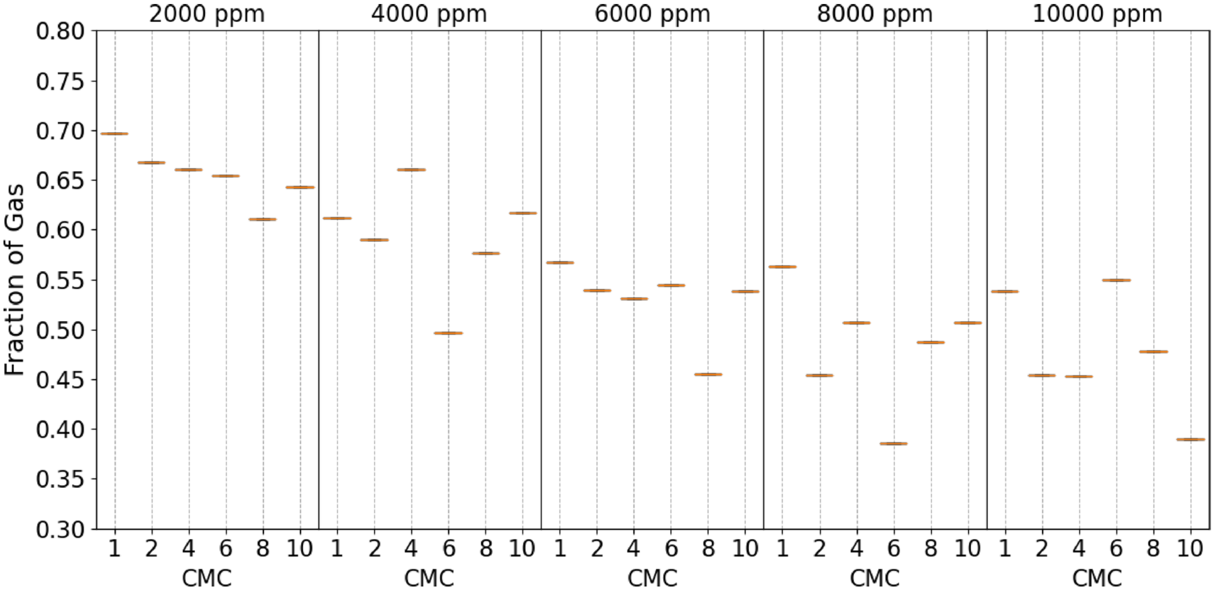

Fig. 7. Initial gas fraction values for 30 concentrations of XG and SDS.

in Supplementary materials. The gas fraction value is relatively high at low XG concentrations, such as 2000 and 4000 ppm. This happens because these concentrations show high mean bubble area values due to low viscosity, allowing larger bubbles to form and move. This can be observed in Figure S1 in Supplementary materials, where CGAs with XG concentrations of 2000 ppm and 4000 ppm exhibit uneven bubble size distribution with many large bubbles present in the image. However, when the concentration of XG exceeds 6000 ppm, the gas fraction value decreases significantly.

The results for the SDS show a diverse range of outcomes. Increasing the SDS concentration at 2000 ppm XG concentration decreases the gas fraction. This trend arises according to the effect of surfactants on bubble formation and growth. Increasing the SDS concentrations leads to increased adsorption at the gas-liquid interface in the solution, which allows the formation of more stable, smaller bubbles with reduced gas retention and coalescence[42]. Changes in SDS concentration do not demonstrate a consistent increasing or decreasing trend for XG concentrations of 4000 ppm and higher.

The middle data points of MBA_0 and Nb_0 at the specified CGA concentrations included in cluster 6a-II from Fig. 6a were selected for further stability analysis. This choice was made based on their uniform bubble formation. Additionally, findings based on the analysis of the MBA and gas fraction at generation are presented below:

- Lower concentrations (1000–2000 ppm) and higher concentrations (10000 ppm) of XG generate bubbles with high MBA values at 0 min.
- Increasing the XG and SDS concentrations leads to a decreasing trend in the gas value fraction. The gas fraction values are the highest for 2000 ppm and 4000 ppm solutions. Also, varying the SDS concentration profoundly affects CGAs with an XG concentration of 2000 ppm.

Effect of SDS and XG concentrations on CGA stability

Figure 8 illustrates the stability of CGAs by comparing the changes in the MBA and Nb over time. Due to their unstable behavior, this plot does not include CGA samples with concentrations of 4 CMC 2000 ppm and all 1000 ppm of XG.

Figure 8a plots the data as the differences in MBA (dMBA) and Nb (dNb) values between 60 min and 0 min. Since the MBA generally increases over time, the difference was calculated by subtracting the MBA value at 0 min from that at 60 min. In contrast, the absolute value of the difference was used for Nb, as the number of bubbles decreased over time.

Overall, cluster 8a-I shows a slight change in bubble area, MBA, and bubble number, Nb, at higher polymer concentrations (6000, 8000 ppm). However, at 2000 ppm within this cluster, bubbles show slow area expansion but experience a notable decrease in bubble number, suggesting reduced stability. CGA fluid samples with higher concentrations of XG have generally exhibited fewer changes in bubble size distribution over time. This stabilization results from increased solution viscosity at higher polymer concentrations, which significantly restricts gas diffusion both into the bulk fluid and between adjacent bubbles[20]thereby preventing bubble growth and coalescence[21]. This occurs as a result of the base fluid's high viscosity, which inhibits air diffusion through the water lamella in the bulk medium. Furthermore, while the base fluid viscosity increases with increasing polymer concentrations, the viscous layer inside aphrons becomes more impenetrable to air diffusion from the gaseous core to the bulk fluid phase[43]. Moreover, at a surfactant concentration of 6 CMC, the bubble area changes insignificantly, and the number of bubbles is almost constant at 6000 and 8000 ppm. In contrast, cluster 8a-II

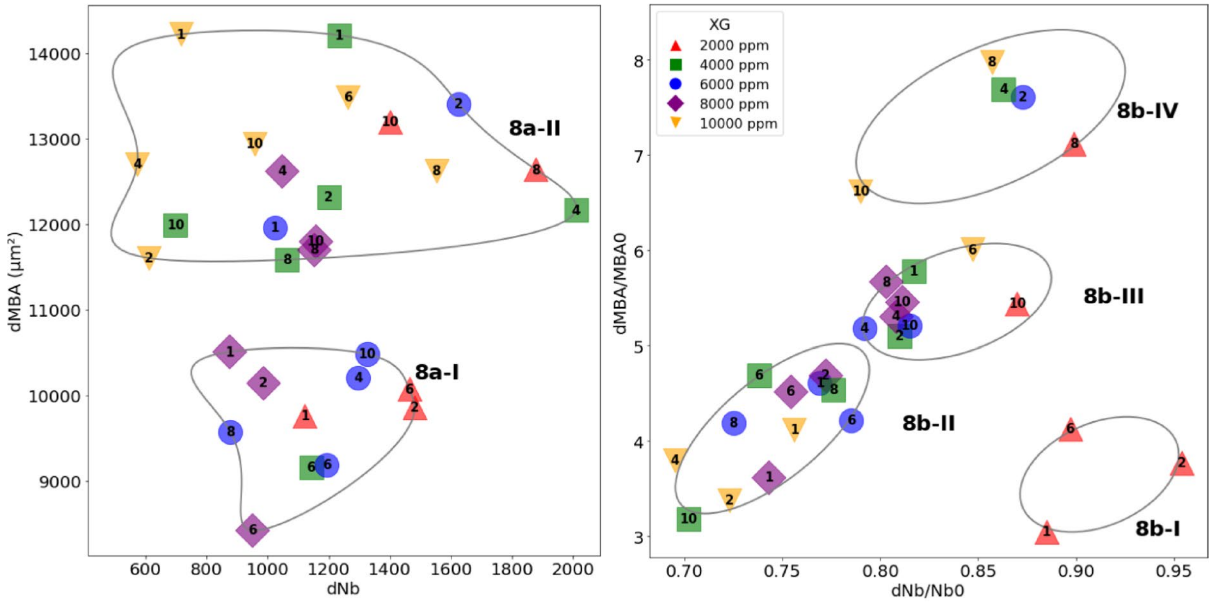

a) b)

Fig. 8. Differences in MBA and Nb values over time for various concentrations of CGA: (**a**) dMBA vs. dNb (**b**) dMBA vs. dNb changed compared to their initial data.

shows notable changes in bubble size and number across the remaining concentrations that were not further considered to determine optimal concentrations. Therefore, the best delta values for MBA and Nb were found at 6 CMC for surfactant, and both polymer concentrations of 6000 and 8000 ppm from cluster 8a-I.

Figure 8b employs identical clustering to categorize the data on change in dMBA and dNb between 60 min and 0 min divided by its initial respective data MBA_0 and Nb_0. In this analysis Fig. 8b provides an understanding of how the mean bubble size changed relative to the initial data, highlighting the bubbles which remain stable after 60 min. The analysis indicates that there are 4 clusters of concentrations based on the degree of change compared to the generation stage.

Cluster 8b-IV shows the greatest change in mean bubble size. It is important to note that 4 out of 5 concentrations in this cluster (2 CMC 6000 ppm, 4 CMC 4000 ppm, 8 CMC 2000 ppm, 8 CMC 10000 ppm) are in cluster 6a-I in Fig. 6a, which describes the data at time = 0 min. It shows that cluster 6a-I indicates concentrations with small mean bubble size and many bubbles at the generation time. In other words, concentrations from 8b-IV with the smallest bubbles at generation (cluster 6a-I) experienced the most significant change, which does not correspond to our definition of stable bubbles. In contrast, the concentrations with the most enormous bubbles at generation showed little difference during 60 min. This pattern is observed in concentrations from cluster 8b-II and cluster 6a-III from Fig. 8b, respectively. In addition, CGAs with 2000 ppm XG in cluster 8b-I tend to show a significant shift in bubble numbers over time compared to the generation stage (Fig. 6a), which does not correspond to the stability behavior. On the other hand, cluster 8b-III shows stable behavior of CGA samples in the presented concentration range since no high rise in MBA or Nb is observed over time regarding their initial values.

The stability of CGA bubbles is balanced between two competing processes: bubble coalescence and collapse (rupture). Bubble coalescence occurs when the thin liquid films separating adjacent bubbles drain to a critical thickness and rupture, leading to the merging of bubbles and a reduction in overall bubble number. This drainage is driven by capillary pressure and gravity, which are countered by film viscosity and surface elasticity[44]. In our system, the presence of XG increases the bulk and interfacial viscosity, thereby slowing down drainage and coalescence. The surfactant SDS further enhances stability by forming adsorbed layers at the gas-liquid interface that reduce surface tension and promote repulsive intermolecular forces, such as electrostatic and steric repulsion, between bubbles. Alternatively, bubble rupture may be caused by shear forces or instabilities at the gas-liquid interface. However, under our static imaging conditions, rupture is minimal. Instead, bubble collapse due to gas diffusion from smaller to larger bubbles (Ostwald ripening) is more relevant[45]. The synergistic use of XG and SDS helps suppress both coalescence and Ostwald ripening, creating a dense viscoelastic barrier that limits gas transport and film thinning. These mechanisms explain the observed differences in MBA and Nb over time among the different CGA formulations.

The size and quantity of the CGA bubbles change over time

Figure 9 demonstrates the MBA growth for all 36 concentrations of the generated CGA over 60 min. The color bar highlights that the MBA ranges from 2500 to 20,000 µm². As MBA rises, the color shifts from blue to red. At some concentrations, all bubbles in the solution collapse before the end of the 60 min because of the

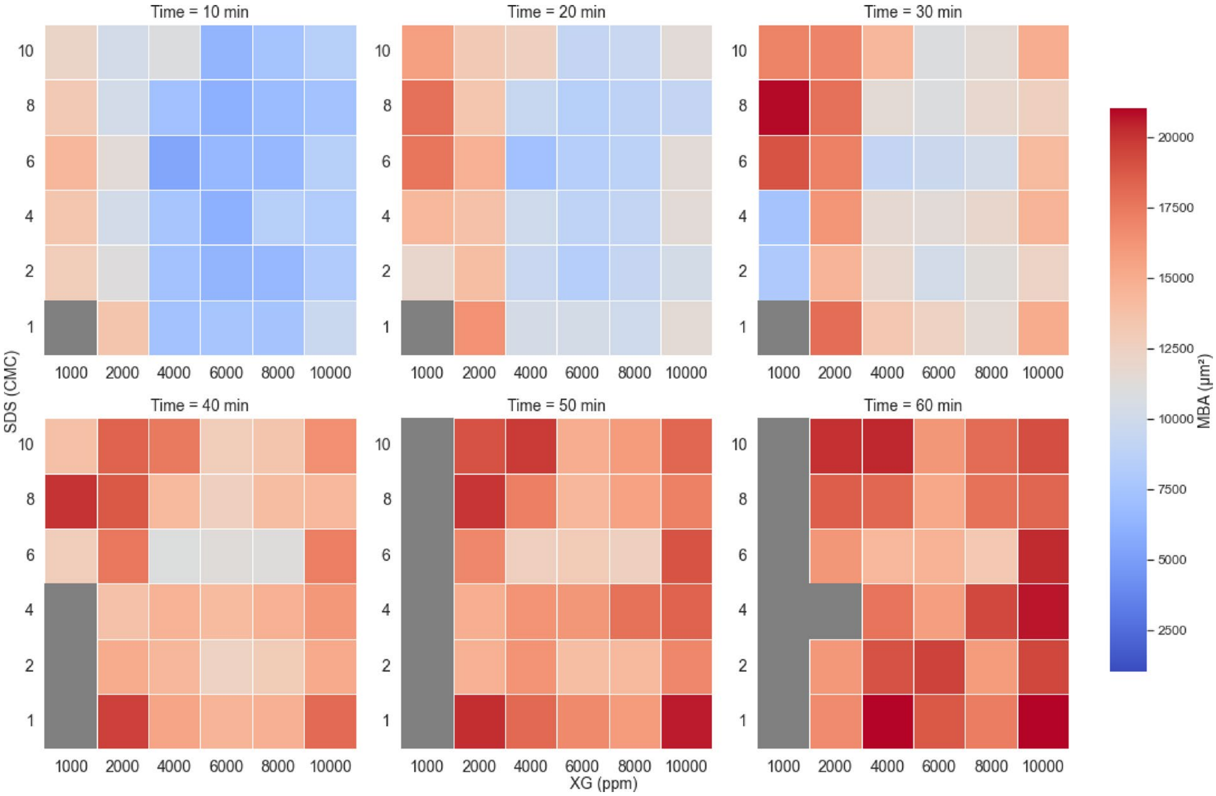

Fig. 9. Color Plot of MBA at 10–60 min for all concentrations of XG and SDS.

higher rate of mean bubble growth. These regions are depicted in gray color. Therefore, we can infer that these concentrations are unstable. Each concentration increases at a different rate, hence, the concentration with the lowest rate of bubble growth would be expected to be the most stable. Concentrations at 10,000 ppm seem to have a more significant MBA each time.

CGA samples prepared with intermediate polymer concentrations (4000, 6000, and 8000 ppm), especially at 6 CMC SDS, showed notably slower bubble growth rates compared to lower and higher XG concentrations. This observation aligns with the findings of Shi et al.[16]who state that at the 6000 ppm of XG, it took about four times longer to reach the same bubble size (160 µm) than for the 2000 ppm of XG. According to that study, which examined concentrations of XG from 1000 to 7000 ppm, the rise in viscosity due to increased XG concentration contributed to the enhanced stability of the CGA samples, explaining the lower rate observed at the 6000 ppm solution in this case. Consequently, the slowest CGA samples in their MBA growth are 6 CMC 4000 ppm, 6 CMC 6000 ppm, and 6 CMC 8000 ppm.

Microscopic images were analyzed to visually assess bubble sizes across all CGA concentrations. This allowed us to check for uneven bubble size distribution at the initial time (Figure S1) and void spaces at the final time (Figure S2 in the Supplementary materials). This procedure is essential because previous image analysis steps focus on characteristics like MBA, which may be similar for bubbles with both even and uneven size distributions, thus overlooking uniformity. For most samples with a concentration of 2000 ppm of XG, the bubble size distribution was not uniform, revealing many large bubbles alongside uniformly distributed tiny bubbles. Notably, nearly half of the bubbles collapsed when the CGAs were analyzed after 60 min. As a result, this concentration and others that displayed similar behavior during the image analysis were excluded from further discussion and consideration. In contrast, all samples at 6000 ppm XG exhibited highly uniform bubble size distributions, indicating greater initial homogeneity and improved overall stability. After 60 min, most bubbles remained stable, and the bubble size distribution in these images was consistent; no void spaces were detected in this sample. This concentration and others exhibiting the same behavior were retained for further analysis.

Consequently, XG concentrations of 1000 & 2000 ppm and SDS concentrations of 1 & 2 CMC were not considered due to the uneven size distribution of bubbles in the CGA samples (see Figure S1). The CGA concentrations from Fig. 6a, cluster 6a-II, and Clusters 8a-I and 8b-III from Fig. 8 that offered more stability with consistent bubbles in area and number were chosen for further investigation. Based on this, the concentrations discovered in all three of the clusters mentioned above, 4 CMC 6000 ppm and 10 CMC 6000 ppm as well as the concentrations found in clusters 6a-II and 8a-I (6 CMC 6000 ppm, 6 CMC 8000 ppm, and 8 CMC 8000 ppm) were chosen from the data of the preceding clusters.

Figure 10 displays the changes of MBA and Nb over 60 min at ten-minute intervals for the five stable CGA samples selected in previous image analysis steps. Error bars represent the 95% confidence intervals (CIs) based on several independent imaging sessions. Results for other concentrations, along with the 95% CIs, are

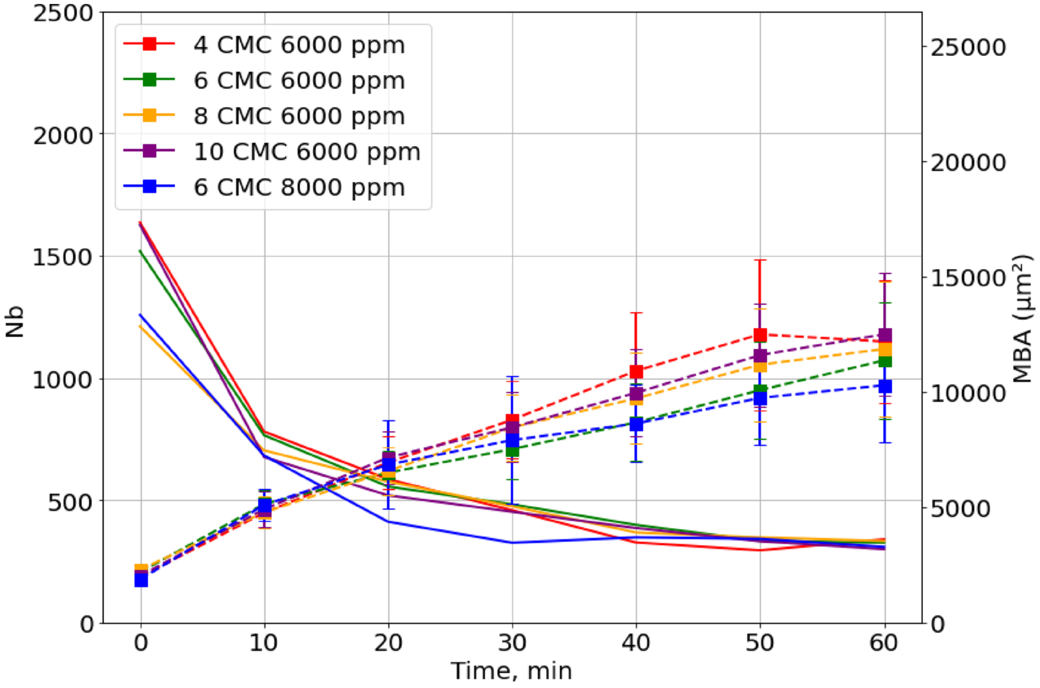

Fig. 10. MBA and Nb change over time for the five most stable CGA systems: 4 CMC 6000 ppm, 6 CMC 6000 ppm, 8 CMC 6000 ppm, 10 CMC 6000 ppm, 6 CMC 8000 ppm.

also presented in Figure S3 of the Supplementary Material. Overall, the MBA increases, as indicated by the dashed lines, whereas Nb decreases due to the coalescence of small bubbles into larger ones, pointing to a loss of bubble stability over time[46]. The comparison of 6000 and 8000 ppm concentrations suggests that a higher XG concentration, such as 8000 ppm, positively affects the bubble growth rate, as a relatively smaller increase in area is observed at the 6 CMC 8000 ppm CGA sample. This can be attributed to the fact that the higher the polymer concentration level, the more the rate of bubble expansion over time is restricted due to the slow diffusion of the highly viscous medium[47]. However, in this sample, the bubble number drops sharply within 60 min, whereas at 6000 ppm, it decreases gradually. Notably, there is no dramatic change during 50 min in bubble size between 6000 and 8000 ppm of XG, particularly at 6 CMC. This suggests that the CGA bubble growth was not significantly affected by increasing the concentration of XG above 6000 ppm, which is consistent with the findings of Shi et al.[16]. Thus, it can be considered that 6000 ppm and 8000 ppm 6 CMC concentrations result in slower bubble growth, while the number of bubbles drops sharply at 8000 ppm 6 CMC concentration. Therefore, 6 CMC 6000 ppm is the most optimal concentration for CGA stability in terms of bubble size and number change over time. There may be some deviations in the number of bubbles at each time step because the image analysis was performed based on images of one certain layer out of 21, and bubbles in the solutions could move in any direction, including the Z axis. Only high-quality images were taken for data analysis, and most of them are not necessarily from the same layer.

The given dataset of CGA growth and stability over time can be characterized using a mathematical model, which captures the trends in bubble behavior. The bubble size distributions of the chosen concentration can be approximated by a Weibull-type distribution[48]:

$$f\left(r;\alpha,\beta\right)=\frac{\alpha}{\beta^{\alpha}}r^{\alpha-1}e^{-\left(\frac{r}{\beta}\right)^{\alpha}}$$

where $f\left(r\right)$ is the probability density function, and the α and β, are the shape parameter and the scale parameter of the distribution, respectively. The bubble area in μm^2 values were transformed into bubble radius in μm values to fit the data into the Weibull-type distribution. The Weibull-type distribution was chosen on the basis of R^2 test[49]where R^2 values outline the degree of variation in a measured outcome explained by the chosen model. The Weibull-type distribution can be chosen as, based on its parameters, it can predict the stability of bubbles over time and their aging process. As we fit the data to this model, we can compare the datasets of different concentrations, which helps us understand the physical dynamics of the process. Hence, we tabulated in Table 2 the fitting values for the α and β parameters along with the coefficient of determination for the five most stable CGA systems.

Figure 11 shows the bubble size distribution for the selected XG and SDS concentrations during image analysis. The bubble size distributions are given for 0 min and 60 min, and high contrast in the shapes of fitting lines for these periods can be noted. At the initial time of 0 min, all five chosen concentrations show that all bubbles fall within the radius range of 5 to 50 μm, consistent with the study by Arabloo and Pordel Shahri[20]which

		α		β		R^2	
Surfactant (CMC)	**Polymer (ppm)**	**0 min**	**60 min**	**0 min**	**60 min**	**0 min**	**60 min**
4	6000	3.319579	2.335644	29.803951	78.772770	0.962600	0.462731
6	6000	3.415823	2.375581	31.558985	70.478493	0.961453	0.646645
	8000	4.133909	2.392660	31.824208	64.705080	0.958249	0.600330
8	6000	3.525828	2.095053	32.882662	69.249267	0.958415	0.614659
10	6000	3.269171	2.538207	29.680461	75.192813	0.965792	0.610625

Table 2. α and β (in μm) values for the Weibull-type distribution equation at 0 min.

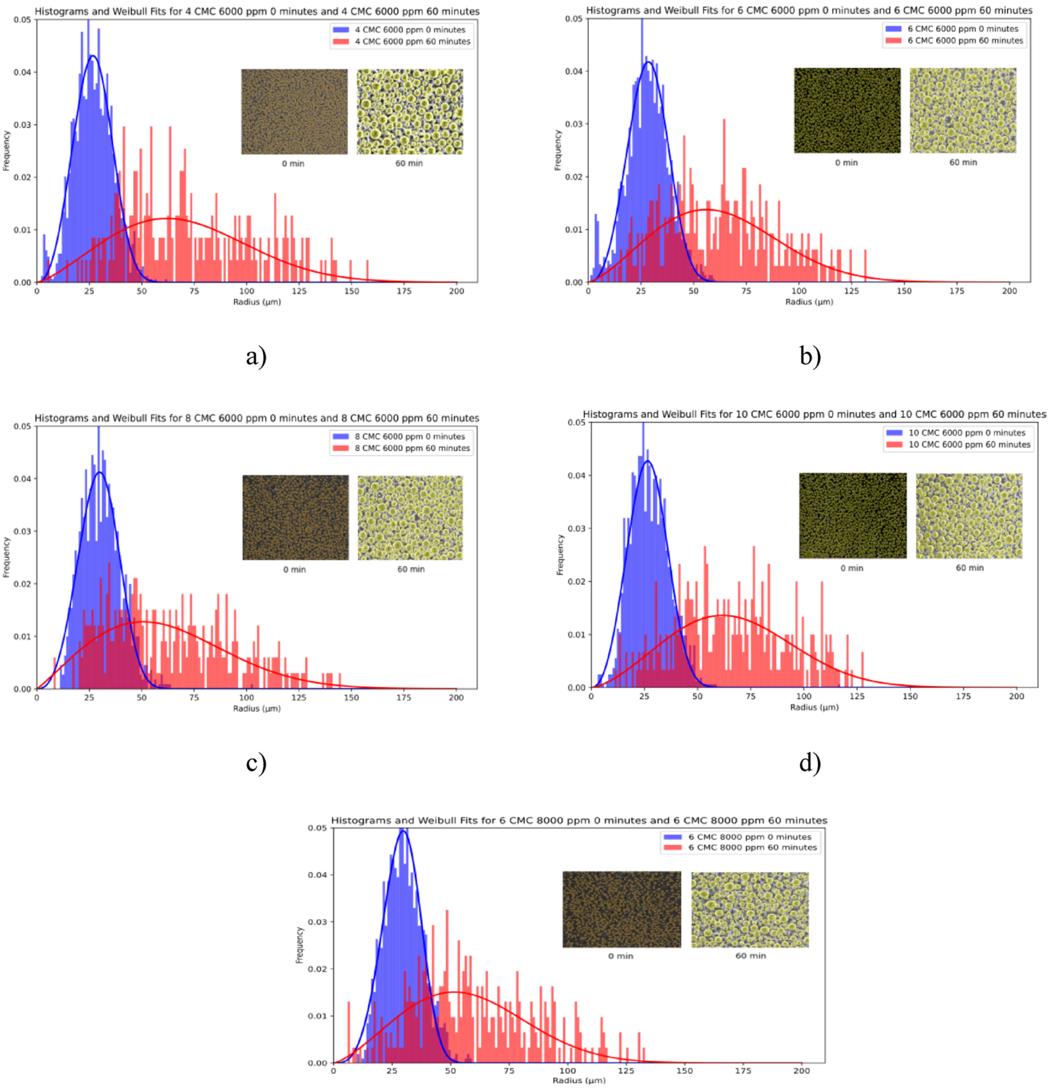

a)

b)

c)

d)

e)

Fig. 11. Bubble size distribution at the initial and final time for: (**a**) 4 CMC 6000 ppm, (**b**) 6 CMC 6000 ppm, (**c**) 8 CMC 6000 ppm, (**d**) 10 CMC 6000 ppm, (**e**) 6 CMC 8000 ppm.

indicated that most CGA bubbles fall within the diameter range of 10 to 100 μm. It is observed that the α coefficient values at 0 min for all concentrations are higher than those at 60 min. All values of α coefficients are larger than 1 for the considered concentrations, which indicates that there is an aging process and the failure rate for considered bubbles increases over time[50]. In contrast, the values of β coefficient at 0 min for varying XG and SDS concentrations are much lower than those at 60 min. Notably, at a concentration of 6 CMC 8000 ppm, the peak of the fitted Weibull line at 0 min reaches a frequency of 0.05, while all other combinations of 6000 ppm reach and surpass the value of 0.04 frequency. Additionally, for the concentration of 6 CMC 8000 ppm at

60 min, the Weibull fitted line exhibits a narrower radius range compared to all other concentrations. A smaller difference between the α and β coefficients at the initial and final time for a given concentration indicates a more stable solution[51]. According to the fitting results, the smallest difference in both α and β coefficients at the initial and final times can be observed for the CGAs at 6 CMC 8000 ppm concentration, which can be determined by calculating the minimum value of the sum of α and β differences.

Thus, from the data presented above, the following conclusions can be drawn:

- Observations indicate that the slowest bubble growth in the CGA sample, in terms of increasing MBA, occurs at 6 CMC 4000 ppm, 6 CMC 6000 ppm, and 6 CMC 8000 ppm.
- However, based on the analysis of microscopic images and a comparison of the behavior of different CGA concentrations over time, the best concentration in terms of bubble size and number change was found to be 6 CMC 6000 ppm.
- Furthermore, the CGA data were fitted to characterize and analyze bubble behavior, stability, and the aging process over time. As a result, at the initial time, the bubble radius values fall within the range of 5–50 μm. This range increases dramatically as the CGAs reach 60 min. According to the fitting results, the most stable concentration, with the smallest difference in both α and β coefficients at the initial and final time, is 6 CMC 8000 ppm.

The optimized CGA formulations identified here (e.g., 6 CMC SDS with 6000 ppm XG) could offer superior performance in practical environmental remediation scenarios. Their enhanced stability and uniform bubble distributions are particularly advantageous for applications such as in-situ soil remediation, where stable gas delivery is essential to sustain aerobic biodegradation of contaminants.

Insights into interfacial dynamics and gas diffusion from MD simulations

Impact of xanthan gum on molecular mobility in CGA systems

To investigate the effects of XG concentration on the mobility of key molecular components in CGA systems, MSD analysis was performed to investigate the influence of XG concentration on the mobility of Na^+ ions, XG, and SDS molecules within a model liquid film. The results, as shown in Fig. 12, reveal that increasing XG concentration restricts molecular motion, where lower MSD slopes indicate reduced diffusion coefficients and constrained particle dynamics, suggesting an increase of the solution viscosity according to the Stokes-Einstein relationship[27].

Na^+ ions and SDS molecules (Fig. 12A and C) showed the highest MSD values in the absence of XG, clearly indicating enhanced molecular mobility and faster diffusion rates without polymer interference. As the XG concentration increased to 24 molecules, the MSD slopes decreased significantly, reflecting reduced diffusion coefficients and hindered motion. This reduction in mobility suggests that the addition of XG introduces steric hindrance and enhances viscosity within the CGA interface, which collectively impede the movement of Na^+ and SDS molecules.

Similarly, the MSD analysis for XG molecules (Fig. 12B) revealed a substantial decrease in molecular motion as the XG concentration increased. While the system containing 8 XG molecules exhibited higher XG mobility, the addition of 16 and 24 XG molecules resulted in significantly lower diffusion rates. This behavior indicates that at higher concentrations, XG molecules form a dense, entangled polymer network that increases the viscosity of the CGA lamella and slows down liquid drainage. This polymer network enhances structural rigidity, contributing to the stability of the bubble films (Xu et al.[25]).

Overall, increased XG concentrations reduce molecular diffusion, thereby significantly enhancing CGA stability. These findings align with density analysis results (Supplementary S4: Figures S7-S9), further confirming the critical role of XG in CGA stabilization.

Gas diffusion in CGA systems: role of XG and SDS

To explore the effects of XG and SDS concentrations on nitrogen (N_2) gas diffusion in CGA systems, we monitored the movement of 30 N_2 molecules from the aqueous layer to the vacuum phase by MD simulations. The percentage of N_2 molecules diffused into the vacuum phase was used as a quantitative measure of gas diffusion, with all 30 molecules considered as 100% (Fig. 13).

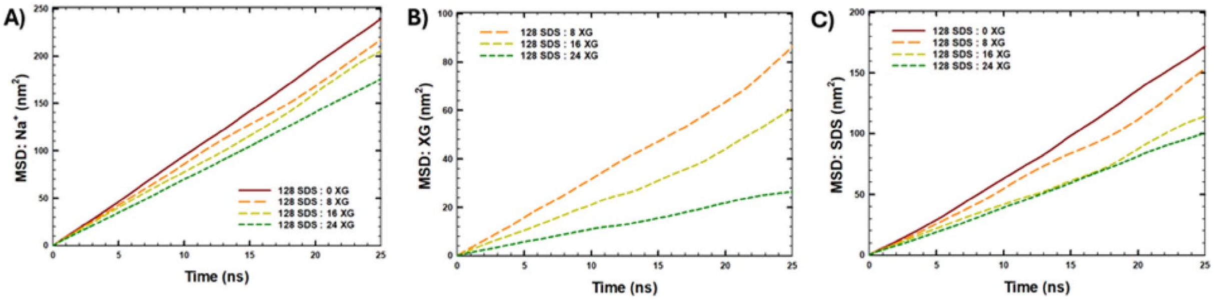

Fig. 12. Mean square displacement (MSD) vs. Time from the production run: (**A**) Na^+ ions, (**B**) XG monomers, and (**C**) SDS molecules.

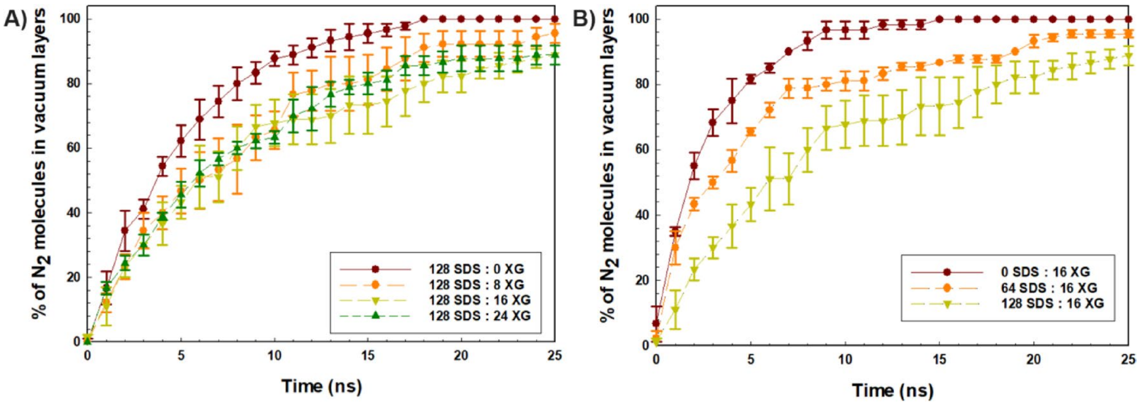

Fig. 13. Percentage of N_2 molecules diffused into the vacuum phase as a function of (**A**) XG concentration and (**B**) SDS concentration. Results are averaged over three simulation runs, with standard error of the mean (SEM) shown as error bars.

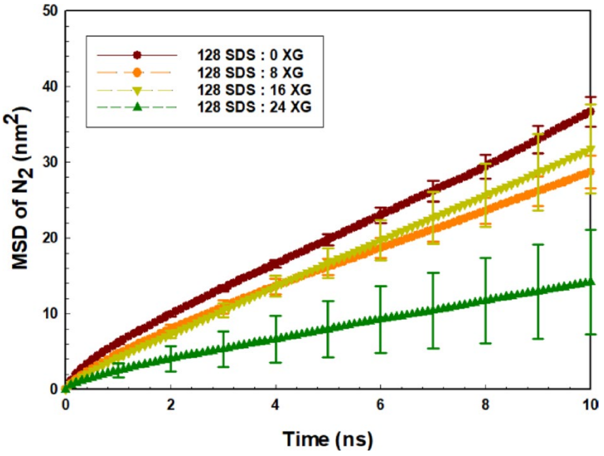

Fig. 14. MSD of N_2 molecules in bulk water at various XG concentrations and constant SDS concentration. Results are averaged over three simulation runs, with SEM shown as error bars.

In the absence of XG, all N_2 molecules diffused into the vacuum phase within 18 ns (Fig. 13A). However, the presence of XG molecules suppressed gas diffusion, with only 86% and 91% of N_2 molecules reaching the vacuum phase by 18 ns and 25 ns, respectively. This suppression effect can be attributed to the increased viscosity and steric hindrance caused by XG, which reduces the mobility of gas molecules.

Similarly, the absence of SDS allowed complete diffusion of N_2 molecules into the vacuum phase within 15 ns (Fig. 13B). The addition of SDS significantly slowed gas diffusion, particularly at the highest concentration of 128 SDS molecules, where only 90% of N_2 molecules diffused into the vacuum phase by 25 ns. This observation suggests that SDS molecules stabilize the CGA interface by forming micelles and reducing gas permeability.

To further investigate N_2 mobility, MSD analysis was conducted for N_2 molecules in a bulk water system at 323 K, with varying XG concentrations and a constant SDS concentration (Fig. 14). The diffusion coefficient of N_2 in the absence of XG was approximately 4.0×10^{-9} m^2/s from our MD simulations. The value is consistent with Ferrell and Himmelblau[52] who reported the diffusion coefficient of N_2 molecules in water of 3.8×10^{-9} m/s at 328 K.

Furthermore, at higher XG concentrations, N_2 mobility was significantly reduced (Fig. 13A), consistent with our earlier observations on the suppressed mobility of Na^+ ions, XG, and SDS molecules in the presence of XG monomers (Fig. 13A). These results highlight the importance of CGA composition in controlling gas diffusion and stabilizing bubble interfaces. Both XG and SDS play critical roles in suppressing gas mobility and improving CGA stability.

Although experimental control cases without XG or SDS could not generate stable CGA structures for image analysis, our MD simulations provided important insights into the individual and combined roles of each component in stabilizing the CGA interface.

Despite the computational constraints that necessitate a simplified MD model, this study provides valuable molecular-level insights into CGA interfaces and the role of XG concentration in interfacial stability. The choice of a 50 ns production run and a $6 \times 6 \times 30$ nm^3 system size strikes a balance between computational feasibility and capturing key interfacial dynamics. While larger systems and longer simulations could offer deeper insights, they come with significant computational costs. To bridge the gap between atomistic simulations and real-world CGA behavior, future studies could integrate coarse-grained or multiscale modeling approaches, combining MD with continuum-scale techniques. Nonetheless, our findings align with experimental observations and contribute to a broader understanding of CGA-based formulations in various applications. Additional visualizations and MD simulation results, including RDFs, density profiles, and detailed snapshots of molecular interactions, are presented in Supplementary Figures S5–S9.

Conclusion

This study uniquely integrates detailed experimental bubble-scale analysis with molecular-level MD simulations, providing novel insights into CGA stability mechanisms. A total of thirty-six CGA samples were assessed, with SDS concentrations ranging from 1 to 10 CMC and XG concentrations from 1000 to 10,000 ppm. Analysis of CGA generation revealed that XG concentrations between 4,000 and 8,000 ppm achieved optimal bubble uniformity and number. These concentrations were found optimal since large bubble formations were observed at low viscosity (1000–2000 ppm), while decreasing in the gas fraction was observed at 10,000 ppm of XG concentration due to the high viscosity of the solution. Among the tested CGA formulations, the most stable were 6 CMC SDS with 6000 ppm XG and 6 CMC SDS with 8000 ppm XG. The first formulation exhibited the slowest increase in bubble size, while the second had the smallest difference between initial and final measurements. These findings highlight the importance of optimizing polymer and surfactant concentrations to achieve optimal CGA stability.

MD simulations provided insights into CGA stabilization mechanisms at the molecular level. The results revealed that higher XG concentrations significantly suppressed molecular mobility, including Na^+ ions, SDS molecules, and XG chains. This suppression was attributed to the viscous liquid film that increased interfacial rigidity and reduced liquid drainage. The results align with experimental trends, offering a deeper understanding of the molecular interactions underlying CGA stability, although the concentrations in MD simulations exceeded experimental values.

This work demonstrates the synergistic effects of surfactant and polymer concentrations on CGA stability by combining experimental data and computational modeling. Advanced image analysis tools enhanced the characterization of bubbles and MD simulations for a better molecular understanding of CGA behavior. The results provide a solid basis for optimizing CGA formulations for applications in soil remediation, enhanced oil recovery, and other areas where stable gas-liquid systems are required.

Future research will focus on validating these findings through column experiments to assess CGA performance in real-world applications such as soil remediation and enhanced oil recovery. In EOR, CGAs might control fluid movement by blocking high-permeability zones and improving sweeping efficiency. Compared to traditional foams, CGAs are less compressible and more stable, making them easier to inject and potentially more effective in deep, high-pressure reservoirs. Future research should also focus on other polymers and surfactants that interact with nonaqueous phase liquids or refine the MD simulations to reproduce the experimental conditions more accurately.

Data availability

The authors declare that the data supporting the findings of this study are available within the paper and its Supplementary Information files. Should any raw data files be needed in another format they are available from the corresponding author upon reasonable request.

Received: 19 February 2025; Accepted: 19 June 2025

References

1. Kazidenov, D. Omirbekov, S., Zhanabayeva, M. & Amanbek, Y. Experimental and numerical study of the effect of polymer flooding on sand production in poorly consolidated porous media. *Geoenerg. Sci. Eng.* **249**, 213746. https://doi.org/10.1016/j.geoen.2025.213746 (2025).
2. Baigadilov, A. et al. Stability and flow behavior of polymer-enhanced foams for improved in-situ remediation of hydrocarbons: Effect of polymer-surfactant interactions. *J. Hazardous Mat.* **486**, 137004. https://doi.org/10.1016/j.jhazmat.2024.137004 (2025).
3. Sabyrbay, B. et al. Assessment of a novel alcohol-in-biopolymer emulsion for enhanced remediation of diesel-contaminated soils. *J. Hazardous Mat. Adv.* **18**, 100616. https://doi.org/10.1016/j.hazadv.2025.100616 (2025).
4. Khatib, Z. I. H. G. J., and A. H. F. Effects of capillary pressure on coalescence and phase mobilities in foams flowing through porous media. *SPE Res. Eng.* **3**(03) (1988).
5. Lake, L. W. *Enhanced Oil Recovery* (Englewood Cliffs, 1989).
6. Maire, J. & Fatin-Rouge, N. Surfactant foam Flushing for in situ removal of DNAPLs in shallow soils. *J. Hazard. Mater.* **321**, 247–255 (2017).
7. Omirbekov, S., Davarzani, H., Colombano, S. & Ahmadi-Senichault, A. Experimental and numerical upscaling of foam flow in highly permeable porous media. *Adv. Water Resour.* **146**, 103761 (2020).
8. Omirbekov, S., Davarzani, H., Sabyrbay, B., Colombano, S. & Ahmadi-Senichault, A. Experimental study of rheological behavior of foam flow in capillary tubes. *J. Non-Newtonian Fluid Mech.* **302**, 104774. https://doi.org/10.1016/j.jnnfm.2022.104774 (2022).
9. Cannella, W. J. H. C. and S. R. S. Prediction of Xanthan Rheology in Porous Media. in *SPE Annual Technical Conference and Exhibition* (Houston, Texas, 1988).
10. Sebba, F. Microfoams—an unexploited colloid system. *J. Colloid Interface Sci.* **35**, 643–646 (1971).
11. Mukhopadhyay, S., Mukherjee, S. & Hashim, M. A. Application of colloidal gas aphron suspensions produced from *Sapindus mukorossi* for arsenic removal from contaminated soil. *Chemosphere* **119**, 355–362 (2015).
12. Muller, K. A., Johnson, C. D., Bagwell, C. E. & Truex, M. J. Methods for delivery and distribution of amendments for subsurface remediation: A critical review. *Groundw. Monit. Remediation*. **41**, 46–75 (2021).

13. Tao, W., Mei, C. & Hamzah, N. The application of surfactant colloidal gas aphrons to remediate contaminated soil: A review. *J. Contam. Hydrol.* **231**, 103620 (2020).
14. Pasdar, M., Kamari, E., Kazemzadeh, E., Ghazanfari, M. H. & Soleymani, M. Investigating fluid invasion control by colloidal gas aphron (CGA) based fluids in micromodel systems. *J. Nat. Gas Sci. Eng.* **66**, 1–10 (2019).
15. Nguyen Hai Le, N., Sugai, Y. & Sasaki, K. Investigation of stability of CO$_2$ Microbubbles—Colloidal gas aphrons for enhanced oil recovery using definitive screening design. *Colloids Interfaces* **4** (2020).
16. Shi, S., Wang, Y., Li, Z., Chen, Q. & Zhao, Z. Laboratory investigation of the factors impact on bubble size, pore blocking and enhanced oil recovery with aqueous colloidal gas aphron. *J. Pet. Explor. Prod. Technol.* **6**, 409–417 (2016).
17. Zhang, M. & Guiraud, P. Surface-modified microbubbles (colloidal gas aphrons) for nanoparticle removal in a continuous bubble generation-flotation separation system. *Water Res.* **126**, 399–410 (2017).
18. Samuel, S. R. & Design, T. J. J. K. E., and development of aqueous colloidal gas aphrons for enhanced oil recovery applications. in *SPE Improved Oil Recovery Symposium* (2012).
19. Keshavarzi, B., Javadi, A., Bahramian, A. & Miller, R. Formation and stability of colloidal gas aphron based drilling fluid considering dynamic surface properties. *J. Pet. Sci. Eng.* **174**, 468–475 (2019).
20. Arabloo, M. & Pordel Shahri, M. Experimental studies on stability and viscoplastic modeling of colloidal gas aphron (CGA) based drilling fluids. *J. Pet. Sci. Eng.* **113**, 8–22 (2014).
21. Pasdar, M., Kazemzadeh, E., Kamari, E., Ghazanfari, M. H. & Soleymani, M. Monitoring the role of polymer and surfactant concentrations on bubble size distribution in colloidal gas aphron based fluids. *Colloids Surf. Physicochem Eng. Asp.* **556**, 93–98 (2018).
22. Corpuz, A. G., Pal, P., Banat, F. & Haija, M. A. Enhanced removal of mixed metal ions from aqueous solutions using flotation by colloidal gas aphrons stabilized with sodium alginate. *Sep. Purif. Technol.* **202**, 103–110 (2018).
23. Zozulya, O. & Pletneva, V. Influence of thermobaric conditions on size distribution of colloidal gas aphrons. *Colloids Surf. Physicochem Eng. Asp.* **483**, 232–238 (2015).
24. Kalesh, D., Merembayev, T., Omirbekov, S & Amanbek, Y. Application of physics-informed neural networks for two-phase flow model with variable diffusion and experimental validation. *Res. Eng.* **26**, 105439. https://doi.org/10.1016/j.rineng.2025.105439 (2025).
25. Xu, C. et al. Improvement of foaming ability of surfactant solutions by Water-Soluble polymers: experiment and molecular dynamics simulation. *Polymers (Basel)* **12** (2020).
26. Du, X. et al. Ultra-stable aqueous foams with multilayer films stabilized by 1-dodecanol, sodium dodecyl sulfonate and polyvinyl alcohol. *Chem. Eng. Sci.* **160**, 72–79 (2017).
27. Wang, Y., Le, X., Wang, X., Liu, W. & Wang, Z. Molecular dynamics simulation of the synergistic effect of alkali/surfactant/polymer on the formation and stabilization of water-based foam systems. *Polymers (Basel)* **15** (2023).
28. Baimaganbetova, S., Omirbekov, S., Wang, Y., Chan, M.-Y. & Talamona D. Investigation of Rheological and Flow Properties of Buckwheat Dough with and Without Xanthan and Guar Gums for Optimized 3D Food Printing Across Temperature Variations. *Foods* **13**(24), 4054. https://doi.org/10.3390/foods13244054 (2024).
29. Abu Elella, M. H. et al. Xanthan gum-derived materials for applications in environment and eco-friendly materials: A review. *J. Environ. Chem. Eng.* **9**, 104702 (2021).
30. Khamehchi, E., Tabibzadeh, S. & Alizadeh, A. Rheological properties of aphron based drilling fluids. *Pet. Explor. Dev.* **43**, 1076–1081 (2016).
31. Zhumabek, M. et al. Stability and rheological characterization of colloidal gas aphrons: influence of xanthan gum and sodium dodecyl sulfate Abstract. *Discover Appl. Sci.* **7**(5), https://doi.org/10.1007/s42452-025-06884-8 (2025).
32. Tabzar, A., Arabloo, M. & Ghazanfari, M. H. Rheology, stability and filtration characteristics of colloidal gas aphron fluids: Role of surfactant and polymer type. *J. Nat. Gas Sci. Eng.* **26**, 895–906 (2015).
33. Biodock & Biodock A. I. Software Platform (2024).
34. Lee, Y., Kim, J., Willette, J., Hwang, S. J. & MPViT Multi-Path Vision Transformer for Dense Prediction. in *Proceedings of the IEEE Computer Society Conference on Computer Vision and Pattern Recognition* (2022).
35. Abraham, M. J. et al. GROMACS: High performance molecular simulations through multi-level parallelism from laptops to supercomputers. *SoftwareX 1–2* **1–2**, 19–25 (2015).
36. Shi, P. et al. Molecular dynamics simulation study of adsorption of anionic-nonionic surfactants at oil/water interfaces. *RSC Adv.* **12**, (2022).
37. Su, L., Sun, J., Ding, F., Gao, X. & Zheng, L. Effect of molecular structure on synergism in mixed zwitterionic/anionic surfactant system: an experimental and simulation study. *J. Mol. Liq.* **322** (2021).
38. Tang, X., Koenig, P. H. & Larson, R. G. Molecular dynamics simulations of sodium dodecyl sulfate micelles in water - the effect of the force field. *J. Phys. Chem. B* **118** (2014).
39. Malde, A. K. et al. An automated force field topology builder (ATB) and repository: Version 1.0. *J. Chem. Theory Comput.* **7**, 4026–4037 (2011).
40. Humphrey, W., Dalke, A. & Schulten, K. VMD: Visual molecular dynamics. *J. Mol. Graph.* **14**, 33–38 (1996).
41. Nsengiyumva, E. M., Heitz, M. P. & Alexandridis, P. Salt and temperature effects on Xanthan gum polysaccharide in aqueous solutions. *Int J. Mol. Sci* **25** (2024).
42. Misyura, S., Morozov, V., Strizhak, P., Shlegel, N. & Donskoy, I. Effect of surfactants on the synthesis and dissociation of gas hydrates. *Fire* **7** (2024).
43. Pasdar, M., Kazemzadeh, E., Kamari, E., Ghazanfari, M. H. & Soleymani, M. Insight into the behavior of colloidal gas aphron (CGA) fluids at elevated pressures: An experimental study. *Colloids Surf. Physicochem. Eng. Asp.* **537**, 250–258 (2018).
44. Tcholakova, S. et al. Role of surface properties for the kinetics of bubble Ostwald ripening in saponin-stabilized foams. *Colloids Surf. Physicochem. Eng. Asp.* **534** (2017).
45. Inoue, S., Kimura, Y. & Uematsu, Y. Ostwald ripening of aqueous microbubble solutions. *J. Chem. Phys.* **157** (2022).
46. Liu, B. et al. Coalescence of bubbles with mobile interfaces in water. *Phys. Rev. Lett.* **122**, 194501 (2019).
47. Xu, F., Cockx, A., Hébrard, G. & Dietrich, N. Mass transfer and diffusion of a single bubble rising in polymer solutions. *Ind. Eng. Chem. Res.* **57**, 15181–15194 (2018).
48. Magrabi, S. A., Dlugogorski, B. Z. & Jameson, G. J. Bubble size distribution and coarsening of aqueous foams. *Chem. Eng. Sci.* **54**, 4007–4022 (1999).
49. Byron, C., Jaeger, L. J. E. & Gurka, M. J. An R2 statistic for covariance model selection in the linear mixed model. *J. Appl. Stat.* **46**, 164–184 (2019).
50. Rinne, H. *The Weibull Distribution: A Handbook* 1st edn (Chapman and Hall/CRC., 2008).
51. Gómez, Y. M., Gallardo, D. I., Marchant, C., Sánchez, L. & Bourguignon, M. An In-Depth Review of the Weibull Model with a Focus on Various Parameterizations. *Mathematics* **12** (2024).
52. Ferrell, R. T. & Himmelblau, D. M. Diffusion coefficients of nitrogen and oxygen in water. *J. Chem. Eng. Data.* **12**, 111–115 (1967).

Acknowledgements

This research is funded by the Science Committee of the Ministry of Science and Higher Education of the Republic of Kazakhstan (Grant No. AP22784980). Special thanks to Prof. Tri Pham and Timur Elebessov from

Nazarbayev University for granting access to the microscopy facilities that were utilized in this research. We also acknowledge research grant no. AP19679429 from the Science Committee of the Ministry of Science and Higher Education of the Republic of Kazakhstan.

Author contributions

A.A., S.K., A.K., and Z.S. wrote the main manuscript text and prepared the figures. A.A., A.K., Z.S., A.I., Y.W., and S.O. contributed to the experimental design, data analysis, and interpretation of the results. M.C., S.C., Y.A., Y.W., and S.O. provided critical revisions to the manuscript. All authors reviewed the final version of the manuscript, approved its claims, and agreed to be authors.

Declarations

Competing interests

The authors declare no competing interests.

Additional information

Supplementary Information The online version contains supplementary material available at https://doi.org/10.1038/s41598-025-08100-4.

Correspondence and requests for materials should be addressed to S.O.

Reprints and permissions information is available at www.nature.com/reprints.

Publisher's note Springer Nature remains neutral with regard to jurisdictional claims in published maps and institutional affiliations.

Open Access This article is licensed under a Creative Commons Attribution-NonCommercial-NoDerivatives 4.0 International License, which permits any non-commercial use, sharing, distribution and reproduction in any medium or format, as long as you give appropriate credit to the original author(s) and the source, provide a link to the Creative Commons licence, and indicate if you modified the licensed material. You do not have permission under this licence to share adapted material derived from this article or parts of it. The images or other third party material in this article are included in the article's Creative Commons licence, unless indicated otherwise in a credit line to the material. If material is not included in the article's Creative Commons licence and your intended use is not permitted by statutory regulation or exceeds the permitted use, you will need to obtain permission directly from the copyright holder. To view a copy of this licence, visit http://creativecommons.org/licenses/by-nc-nd/4.0/.

© The Author(s) 2025